JYX
JYVÄSKYLÄN YLIOPISTO
UNIVERSITY OF JYVÄSKYLÄ

This is a self-archived version of an original article. This version may differ from the original in pagination and typographic details.

Author(s): Collins, Richard; José Heras Ojea, Maria; Mansikkamäki, Akseli; Tang, Jinkui; Layfield, Richard A.

Title: Carbonyl Back-Bonding Influencing the Rate of Quantum Tunnelling in a Dysprosium Metallocene Single-Molecule Magnet

Year: 2020

Version: Accepted version (Final draft)

Copyright: © 2020 American Chemical Society

Rights: In Copyright

Rights url: http://rightsstatements.org/page/InC/1.0/?language=en

Please cite the original version:

Collins, R., José Heras Ojea, M., Mansikkamäki, A., Tang, J., & Layfield, R. A. (2020). Carbonyl Back-Bonding Influencing the Rate of Quantum Tunnelling in a Dysprosium Metallocene Single-Molecule Magnet. Inorganic Chemistry, 59(1), 642-647. https://doi.org/10.1021/acs.inorgchem.9b02895

Carbonyl Back-bonding Influences the Rate of Quantum Tunnelling in a Dysprosium Metallocene Single-Molecule Magnet

Richard Collins,[a,b] *Maria-Jose Heras-Ojea,*[a] *Akseli Mansikkamäki,**[c]

*Jinkui Tang,**[d] *Richard A. Layfield**[a]

a Department of Chemistry, School of Life Sciences, University of Sussex, Brighton, BN1 9QR, U.K.

b School of Chemistry, The University of Manchester, Oxford Road, Manchester, M13 9PL, U.K.

c Department of Chemistry, Nanoscience Centre, University of Jyväskylä, P. O. Box 35, FI-40014, Finland.

d State Key Laboratory of Rare Earth Resource Utilization, Changchun Institute of Applied Chemistry, Chinese Academy of Sciences, Changchun 130022, P.R. China.

ABSTRACT

The isocarbonyl-ligated metallocene coordination polymers $[Cp^*_2M(\mu\text{-}OC)W(Cp)(CO)(\mu\text{-}CO)]_\infty$ were synthesized with M = Gd (**1**) and Dy (**2**). In zero DC field, the dysprosium version **2** was found to be an SMM, with an analysis of the dynamic magnetic susceptibility data revealing that the axial dysprosium coordination environment leads to a large anisotropy barrier of 583 cm^{-1} and a fast quantum tunneling rate of ~2 ms. Theoretical analysis of two truncated versions of **2**, $[Cp^*_2Dy\{(\mu\text{-}OC)W(Cp)(CO)_2\}_2]^-$ (**2a**) and $[Cp^*_2Dy(OC)_2]^+$ (**2b**), in which the effects of electron correlation outside of the 4f orbital space were studied, revealed that tungsten-to-carbonyl back donation plays an important role in determining the strength of the competing equatorial field at dysprosium and, hence, the dynamic magnetic properties. The finding that a classical organometallic bonding scenario could be used as an indirect way of tuning the rate of quantum tunneling in isocarbonyl-ligated SMMs potentially provides an alternative chemical strategy for the design of molecular spin qubits.

The magnetic bistability found in molecular materials such as main-group radicals,[1] spin-crossover compounds[2,3] and single-molecule magnets (SMMs)[4–9] has led to proposals for using this property as the basis of switchable devices such as optical displays, sensors and magnetic memory applications. In the case of SMMs, the bistability is manifested in the dependence of the magnetization on the applied magnetic field, which shows hysteresis up to a characteristic blocking temperature (T_B). The timescales on which SMMs flip their magnetization from one state to another have been the subject of considerable interest in recent years, with slow relaxation of the magnetization informing the development of magnetic information storage materials, whereas fast relaxation via quantum-tunneling of the magnetization (QTM) is relevant to the design of molecular spin qubits for quantum computing.[10,11]

From a fundamental perspective, SMMs continue to reveal a great deal about how the electronic structure and chemical bonding in compounds of transition metals, lanthanides and actinides can be manipulated at the molecular level. A major goal is to increase T_B and the effective energy barrier to reversal of the magnetization (U_{eff}), which can be achieved by, for example, targeting highly axial coordination environments[12–14] or using exchange coupling to enhance the magnetic blocking.[15,16] As a result, many compounds with large energy barriers and impressive hysteresis properties are known,[17–20] with the current benchmark being the dysprosium metallocene $[(Cp^*)Dy(C_5{}^iPr_5)][B(C_6F_5)_4]$ (Cp* = pentamethylcyclopentadienyl), which has a U_{eff} of 1540 cm^{-1} and a T_B of 80 K.[21]

Whilst strategies for influencing SMM performance usually focus on the primary coordination environment of the spin-bearing centre, evidence is available to support the notion that more

remote ligand-based effects also impact on the properties. For instance, Murugesu *et al*. have shown that the barriers in a series of phenoxo-bridged Dy_2 SMMs can be changed by including electron-withdrawing substituents on the ligand periphery, the result of which is to reduce the charge on the coordinating atoms and, hence, alter the crystal field experienced by the lanthanide.[22] Intrigued by observations such as these, we were interested to see if a similar effect could be produced in a dysprosium metallocene SMM in which the equatorial positions are occupied by the oxygen atoms of a transition metal isocarbonyl fragment. Since the synergic back-bonding between a 5d transition metal and a CO ligand should be stronger than with a 3d metal, a greater build-up of negative charge on oxygen can be anticipated in the former case and, hence, the anisotropy barrier should decrease and the rate of QTM should increase. To investigate this idea, we aimed to synthesize a dysprosium metallocene SMM in which the Dy^{3+} ions are bridged by the isocarbonyl ligands of $[CpW(CO)_3]^-$, which formally contains a tungsten(0) centre. The target compound was obtained through the reaction of $[Cp^*_2Dy][BPh_4]$ with $Na[CpW(CO)_3]$ according to Scheme 1.

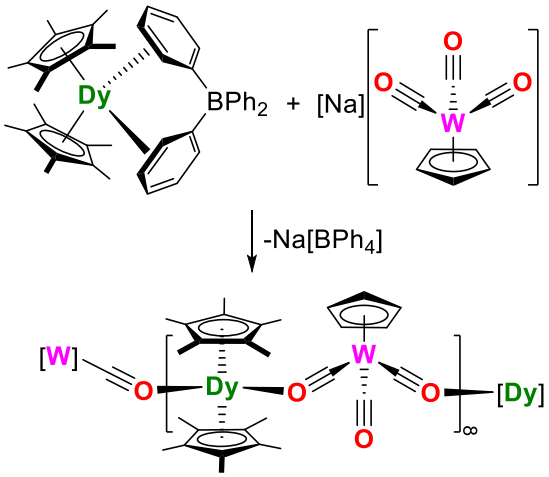

Scheme 1. Synthesis of **2** showing a segment of the polymeric structure.

To demonstrate the generality of the synthetic method, the analogous reactions with yttrium and gadolinium were also undertaken. The products of the three reactions were identified by X-ray crystallography to be the coordination polymers [{Cp^*_2Gd(μ-OC)W(Cp)(CO)(μ-CO)}{Cp^*_2Gd(THF)(μ-OC)W(Cp)(CO)(μ-CO)}]$_\infty$ (**1**) and [Cp^*_2Dy(μ-OC)W(Cp)(CO)(μ-CO)]$_\infty$ (**2**), which were isolated in yields of 39-49% (Tables S1-S3). The repeat unit in the two isostructural compounds consists of a bent lanthanide metallocene with two η^5-Cp* ligands, with the oxygen atoms of two isocarbonyl ligands forming {M–OC–W} bridges to neighbouring tungsten atoms (Figures 1, S3, S4). Two carbonyl ligands in each $[CpW(CO)_3]^-$ unit therefore bridge to different lanthanides, whereas the third carbonyl ligand is terminally bound to tungsten. For **2**, the Dy–Cp* distances are 2.34534(8) and 2.34805(6) Å, the Cp*-Dy-Cp* angle is 138.74(13)°, and the Dy–O distances and O-Dy-O angle are 2.303(6) and 2.308(7) and 85.3(3)°, respectively. The C–O distances of the μ-isocarbonyl ligands in **2** are 1.178(11) and 1.204(3) Å and, hence, slightly longer than the analogous distance of 1.16754(3) Å in the non-bridging CO ligand. The asymmetry in the carbonyl bonding is reflected in the infrared spectrum of **2**, which features absorptions at 1615 and 1726 cm^{-1} for the isocarbonyl ligands and at 1917 cm^{-1} for the terminal carbonyl ligand (Figure S2). The structure of compound **1** is similar to that of **2** in that it consists of chains of {Cp^*_2Gd(μ-OC)W(Cp)(CO)(μ-CO)} units, but with the gadolinium centre in every other unit also being bound to a THF ligand (Figures S3, S4). Compound **1** also has a similar IR spectrum to **2** (Figures S1).

The temperature-dependence of the magnetic susceptibility (χ_M) of **1** and **2** was measured in a static (DC) field of 1000 Oe, with the results being typical of compounds containing isolated Gd^{3+} and Dy^{3+} ions with $^8S_{7/2}$ and $^6H_{15/2}$ ground terms, respectively (Figures S5-S7).[23] In the case of **1**, the value of $\chi_M T$ at 300 K is 7.66 cm^3 K mol^{-1} and only a weak temperature dependence is observed

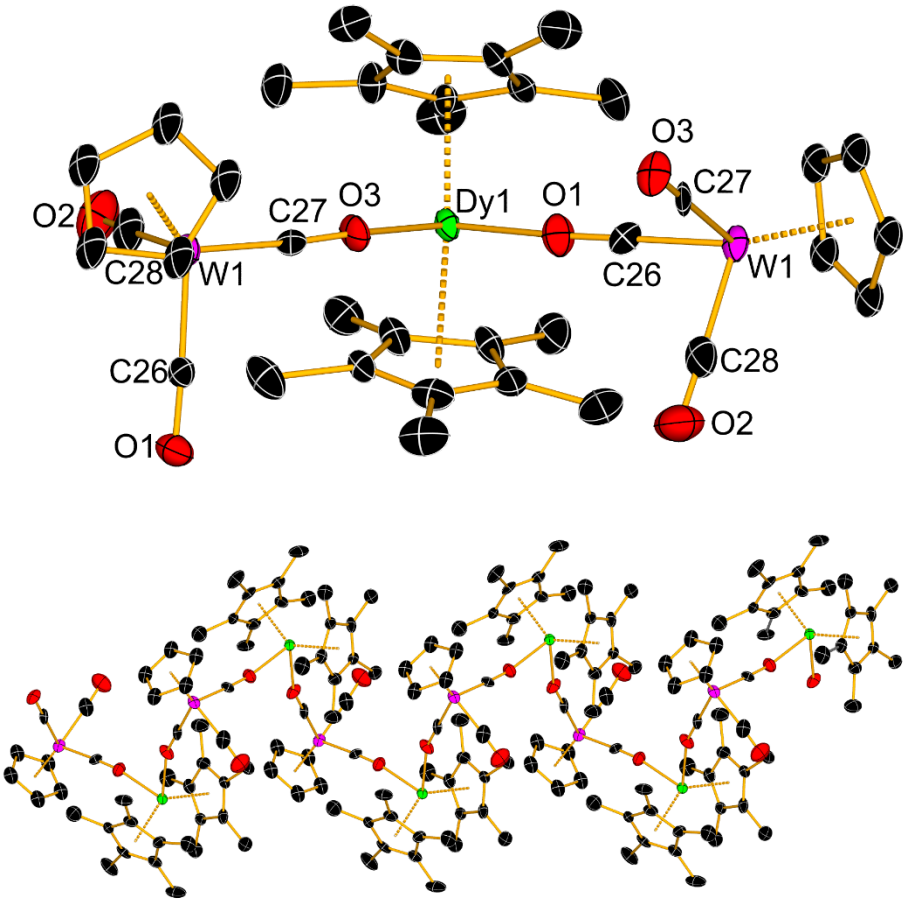

Figure 1. Upper: the repeat structural unit in **2**. Lower: an extended section of the coordination polymer structure. Thermal ellipsoids set to 50% probability.

down to 2 K. The slight decrease in $\chi_M T$ at low temperatures may be due to a weak intra-chain antiferromagnetic interaction between nearest neighbour gadolinium centres. An accurate fit of the data was possible using PHI according to the equation stated in the SI, using g = 1.99 and an exchange term z_j = –0.001 cm^{-1}.[24] From a $\chi_M T$ value of 12.39 cm^3 K mol^{-1} at 300 K, the $\chi_M T(T)$ profile for **2** reveals a slightly more pronounced decreases as the temperature is lowered, with a marked drop occurring at 10 K to reach at 10.92 cm^3 K mol^{-1} 2 K, reflecting thermal depopulation of the higher-lying crystal field states in the ground spin-orbit-coupled multiplet (Figure S7).[25]

The SMM properties of **2** were established using AC magnetic susceptibility measurements, with an oscillating field of 3 Oe and zero applied DC field. The frequency-dependence of the imaginary component of the AC susceptibility, i.e. $\chi''(\nu)$ was measured at various temperatures in the range 1.9-52 K, with clear maxima observable up to 45 K (Figures 2, S8).

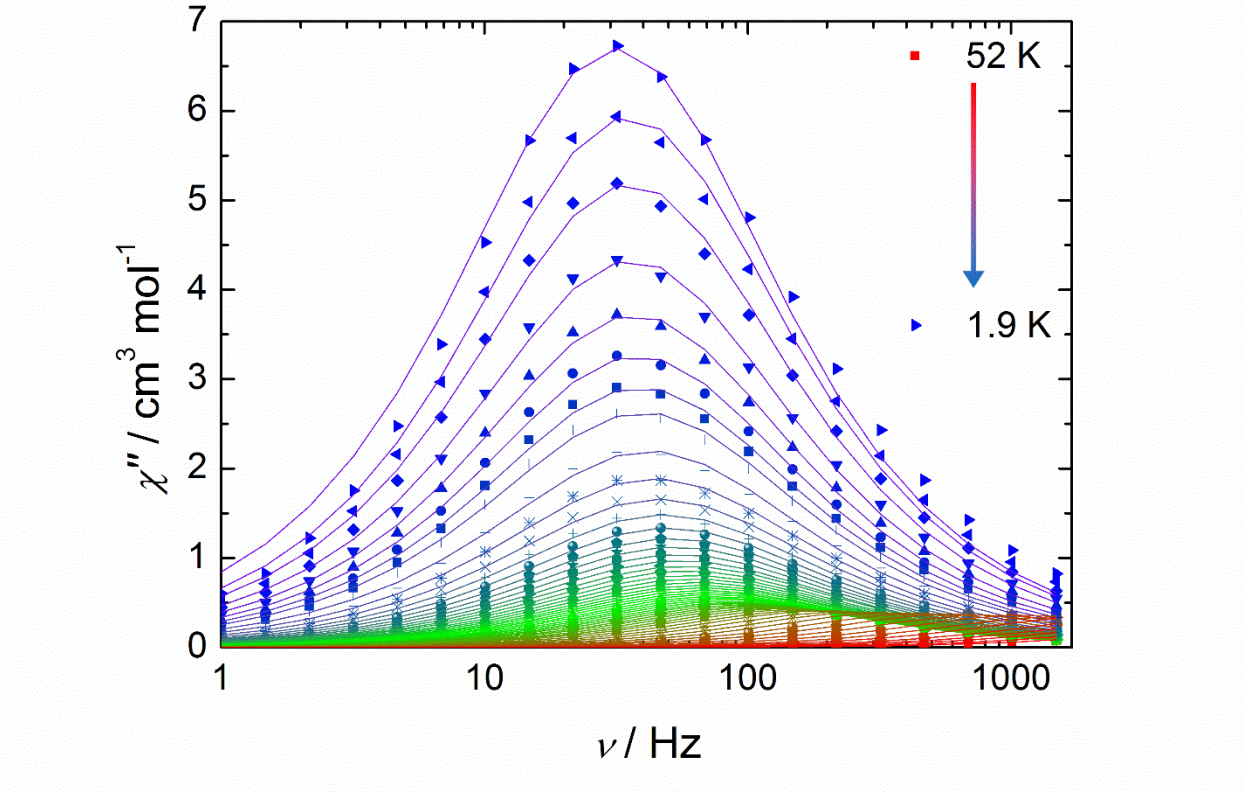

Figure 2. Frequency dependence of χ''_M in **2** in the temperature range 1.9-52 K, using zero applied DC field and an AC field of 3 Oe.

Varying the temperature in the range 1.9-21 K, the frequency of the maximum in χ'' does not shift appreciably, which is indicative of relaxation via quantum tunneling of the magnetization (QTM). At higher temperatures, the maximum in χ'' moves to higher frequencies owing to the onset of a thermally activated relaxation process. A Cole-Cole plot of χ'' versus χ' (the real

component of the AC susceptibility) produced parabola-shaped curves that were fitted using *a*-parameters in the range 0-0.148, implying a fairly narrow range of relaxation times (Figure S9). The temperature dependence of the relaxation times (τ), as extracted from fits of the AC susceptibility data, were then plotted as $\tau^{-1}(T)$, which confirmed that the relaxation time is essentially temperature independent up to 40 K, and then an abrupt increase shows that τ is strongly temperature dependent up to 52 K (Figure S10). A fit of this data was possible using $\tau^{-1} = \tau_0^{-1} e^{-U_{\mathrm{eff}}/k_{\mathrm{B}}T} + CT^n + \tau_{QTM}^{-1}$, in which τ_0 is the pre-exponential factor, C is the Raman coefficient, n is the Raman exponent and τ_{QTM} is the rate of QTM. The fit yielded U_{eff} = 583 cm^{-1}, $\tau_0 = 1.44 \times 10^{-12}$ s, C = 1.56×10^{-9} s^{-1} K^{-n}, n = 2.62 and τ_{QTM} = 1.97 ms. The anisotropy barrier determined for **2** is relatively large and characteristic of a dysprosium metallocene SMM and markedly larger than the barrier of 12.6 cm^{-1} determined for the monometallic isocarbonyl-ligated SMM [{CpW(CO)$_2$(μ-CO)}$_3$Dy(thf)$_5$] in an applied field of 400 Oe.[26] In comparison to the dimetallic isocarbonyl-ligated SMM [Cp*$_2$Dy(μ-Fp)]$_2$, which has U_{eff} = 662 cm^{-1} and τ_{QTM} = 230 ms,[27] the barriers are similar, however the rate of QTM for **2** is almost two orders of magnitude faster. Furthermore, the rate of QTM in **2** is almost seven orders magnitude faster than in [(Cp*)Dy(C$_5$^{i}Pr$_5$)][B(C$_6$F$_5$)$_4$],[21] thus highlighting the sensitivity of the dynamic magnetic properties of dysprosium metallocenes to changes in the chemical environment. The Raman exponent determined for **2** is also quite small relative to the typical values of n = 7-9 for dysprosium; however, small Raman exponents are seemingly common for dysprosium metallocene SMMs, which is currently thought to be related to the vibrational modes associated with cyclopentadienyl ligands.[9,19,21,27,28] The very fast QTM in **2** suggests that the material should show weak magnetic hysteresis, which was confirmed by the measurement of narrow, S-shaped magnetization vs. field loops at 1.9 K when using a scan rate of 28 Oe s^{-1} (Figure S11).

Magneto-structural correlations have been developed to explain and predict the properties of dysprosium metallocene SMMs and related materials. On this basis, the parameters describing **2** imply a highly axial crystal field arising from the Cp* ligands, which explains the large U_{eff} value, but also a non-negligible equatorial component to explain the fast QTM and weak hysteresis, which must be due to the isocarbonyl ligands. Quantitative support for this explanation was provided by an ab-initio computational study in which the geometry of **2** was extracted from the crystal structure and truncated for the multireference calculations, with one Cp^*_2Dy unit, two CpW units connected to dysprosium via the isocarbonyl ligands, and all CO ligands coordinated to the two tungsten atoms, *i.e.* $[Cp^*_2Dy\{(\mu\text{-}OC)W(Cp)(CO)_2\}_2]^-$ (**2a**) and (Figure 3). The positions of hydrogen atoms were optimized using density functional theory and the electronic structure was modeled at the SA-CASSCF(9,7)//SO-RASSI level (see SI for computational details).[29–35]

The energies and principal components of the **g**-tensors of the eight lowest Kramers doublets (KDs) arising from the crystal-field split $^6H_{15/2}$ ground multiplet for the Dy^{3+} ion are listed in Table S4. The **g**-tensor of the ground doublet is strongly axial (g_x = 0.0010, g_y = 0.0019, g_z = 19.5176), which should significantly reduce ground-state QTM. The principal magnetic axis of the ground KD is approximately oriented towards the centre of each Cp* ligand (Figure 3).

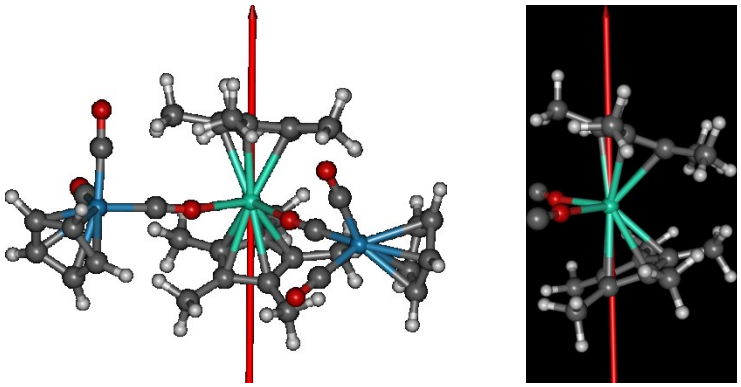

Figure 3. The principal magnetic axis of the ground Kramers doublet of **2a** (left) and **2b** (right).

The axiality of the other **g** tensors steadily decreases in the excited KDs as one moves to higher energy. The relatively large transverse components of the **g** tensor of the second-excited KD (g_x = 0.6487, g_y = 0.9806, g_z = 14.2336) should allow significant temperature-activated QTM. Furthermore, the principal axes of the three lowest doublets are roughly collinear, but the axis of the third excited doublet is almost perpendicular to the axis of the ground doublet. This feature of the electronic structure allows significant spin-phonon transitions and the barrier should be crossed at this point, resulting in an effective barrier of 386 cm^{-1} for the Orbach process. An approximate relaxation route was then constructed for **2a** using previously established methodology, where the relaxation pathway is obtained by tracing the path set by largest transition moment matrix elements between the different electronic states. The barrier is shown in Figure 4 and the numerical values of the transition magnetic moments and the squared projections of the states in the eight lowest KDs on the angular momentum states $|JM_J\rangle$ with J = 15/2 are given in Table S5 and S6, respectively.

The calculation predicts relaxation via the third excited doublet, in agreement with the information obtained from the **g** tensors. However, the barrier predicted by the multireference calculations is considerably lower than the value 583 cm^{-1} obtained from a fit to the experimental data. Whilst the sixth and seventh excited KDs at 494 cm^{-1} and 696 cm^{-1}, respectively, do encompass this barrier, the direction of the principal magnetic axes in these doublets are considerably skewed relative to the ground KD and the fifth-excited KD has a very strong transverse component to the g tensor (g_x = 3.8030, g_y = 6.7534, g_z = 10.1946). Hence, it is extremely unlikely that the relaxation would take place via these higher excited states.

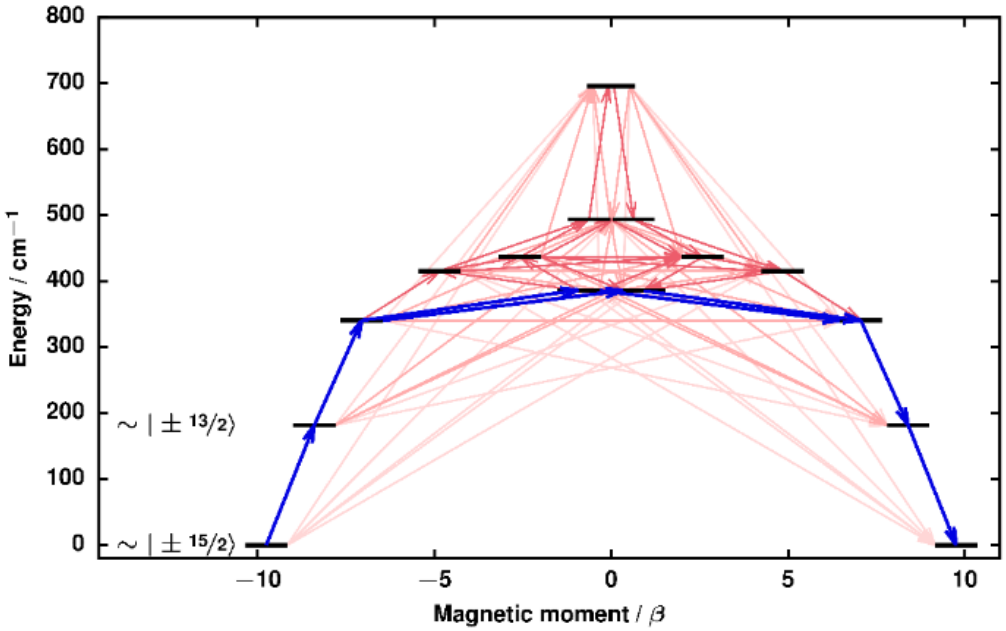

Figure 4. The *ab initio* blocking barrier constructed for **2a**. The blue arrows indicate the most probable relaxation route. Stronger red color in the other arrows indicates a stronger transition magnetic moment.

The discrepancy most likely originates from the neglect of electron correlation effects outside the 4f orbital space; more specifically, from an inaccurate description of the tungsten-to-carbonyl back donation. To confirm this, a Hartree–Fock (HF) calculation, which neglects all electron correlation effects, and a hybrid DFT calculation which accounts for electron correlation effects were carried out on a closed-shell, 18-electron $[CpW(CO)_3]^-$ fragment. Effective atomic charges were then calculated for the atoms using the LoProp approach.[36] The effective charge of the tungsten atom changes slightly from 0.33 in the HF calculation to 0.34 in the hybrid DFT calculation, whereas the charges of the carbonyl carbon atoms change from 0.20, 0.20 and 0.22 to 0.10, 0.10 and 0.12 and the charges of the oxygen atoms change from –0.50, –0.51 and –0.47 to –0.41, –0.41 and –0.38. These values demonstrate that neglecting electron correlation in the W–CO interaction leads

to overestimation of the charge polarization of the CO ligand and to an excessively negative charge on the oxygen atoms. In turn, this leads to an overestimation of the equatorial component of the crystal field in **2**, which explains why the effective barrier height is underestimated in the calculations.

To provide further insight into the effects of tungsten-to-carbonyl back-donation on the magnetic properties of Dy^{3+}, the calculations performed on **2a** were repeated on the simpler model system $[Cp^*_2Dy(OC)_2]^+$ (**2b**) where the absence of tungsten atoms removes all back-donation effects. The energies and properties of the eight lowest KDs of **2b** and the calculated ab initio crystal field parameters are listed in Tables S8 and S9. The principal magnetic axis of the ground KD in **2b** is almost collinear with the corresponding axis in **2a** (Figure 3). It is clear from the principal components of the **g** tensors that the crystal field around Dy^{3+} in **2b** is more axial than in **2a**. The transverse components of the **g** tensor of the ground KD are an order of magnitude smaller in **2b** than in **2a** and the principal axes of the excited KDs have much smaller angles with respect to the axis of the ground doublet. A significant angle between the axes is not observed until the fourth excited doublet, compared to the third excited doublet in **2a**. In contrast to **2a**, the most probable relaxation route for **2b** is predicted via the fifth excited doublet, giving a much larger effective barrier of 805 cm^{-1}. There is, however, moderately strong thermally assisted QTM also takes place at the third and fourth excited doublets, which implies that the relaxation may be faster than the barrier height suggests.

Finally, further computational evidence for the impact of tungsten-to-carbonyl back bonding on the magnetic axiality of the dysprosium metallocene unit was obtained from the calculated ab initio

crystal field parameters in **2a** and **2b**.[37] The results reveal a much higher degree of axiality in **2b** since the axial parameter B_{20} is 86% larger than in **2a** and the B2±2 parameters are smaller (Tables S7 and S9).

In conclusion, the isocarbonyl-ligated rare-earth metallocenes **1** and **2** have been synthesized and the dysprosium version **2** found to be an SMM with a large thermal anisotropy barrier of 583 cm^{-1} in zero DC field. A fast rate of QTM was also determined for **2** owing to the influence of the isocarbonyl ligands, which generate an appreciable equatorial crystal field at the lanthanide owing to strong tungsten-to-carbonyl back-bonding. These results imply that classical bonding motifs in transition metal organometallic chemistry can provide a way of tuning of the QTM rate in lanthanide SMMs, which may be of use in the design of molecular spin qubits.

ASSOCIATED CONTENT

Supporting Information

Synthesis details, analytical characterization including X-ray crystallography and CIF files, magnetic property measurements and computational details. This material is available free of charge via the Internet at http://pubs.acs.org.

AUTHOR INFORMATION

Corresponding Author

akseli.mansikkamaki@jyu.fi

tang@ciac.ac.cn

r.layfield@sussex.ac.uk

Author Contributions

The manuscript was written through contributions of all authors. All authors have given approval to the final version of the manuscript.

Notes

The authors declare no competing financial interests.

ACKNOWLEDGEMENT

JT and RAL thank the Royal Society for a Newton Advanced Fellowship (NA160075). We also thank the ERC (CoG 646740), the EPSRC (EP/M022064/1), the Magnus Ehrnrooth Foundation, the CSC-IT Center for Science in Finland, the Finnish Grid and Cloud Infrastructure (urn:nbn:fi:research-infras-2016072533), and Prof. H. M. Tuononen (University of Jyväskylä) for computational resources.

REFERENCES

(1) Preuss, K. E. Metal-Radical Coordination Complexes of Thiazyl and Selenazyl Ligands. *Coord. Chem. Rev.* **2015**, *289–290*, 49–61. https://doi.org/https://doi.org/10.1016/j.ccr.2014.09.016.

(2) Meng, Y.-S.; Liu, T. Manipulating Spin Transition To Achieve Switchable Multifunctions. *Acc. Chem. Res.* **2019**, *52* (5), 1369–1379. https://doi.org/10.1021/acs.accounts.9b00049.

(3) Kumar, K. S.; Ruben, M. Emerging Trends in Spin Crossover (SCO) Based Functional Materials and Devices. *Coord. Chem. Rev.* **2017**, *346*, 176–205. https://doi.org/https://doi.org/10.1016/j.ccr.2017.03.024.

(4) Guo, F.-S.; Bar, A. K.; Layfield, R. A. Main Group Chemistry at the Interface with Molecular Magnetism. *Chem. Rev.* **2019**. https://doi.org/10.1021/acs.chemrev.9b00103.

(5) Liu, J.-L.; Chen, Y.-C.; Tong, M.-L. Symmetry Strategies for High Performance Lanthanide-Based Single-Molecule Magnets. *Chem. Soc. Rev.* **2018**, *47* (7), 2431–2453.

https://doi.org/10.1039/C7CS00266A.

(6) Zhu, Z.; Guo, M.; Li, X.-L.; Tang, J. Molecular Magnetism of Lanthanide: Advances and Perspectives. *Coord. Chem. Rev.* **2019**, *378*, 350–364. https://doi.org/10.1016/J.CCR.2017.10.030.

(7) Harriman, K. L. M.; Murugesu, M. An Organolanthanide Building Block Approach to Single-Molecule Magnets. *Acc. Chem. Res.* **2016**, *49* (6), 1158–1167. https://doi.org/10.1021/acs.accounts.6b00100.

(8) Frost, J. M.; Harriman, K. L. M.; Murugesu, M. The Rise of 3-d Single-Ion Magnets in Molecular Magnetism: Towards Materials from Molecules? *Chem. Sci.* **2016**, *7* (4), 2470–2491. https://doi.org/10.1039/C5SC03224E.

(9) Day, B. M.; Guo, F.-S.; Layfield, R. A. Cyclopentadienyl Ligands in Lanthanide Single-Molecule Magnets: One Ring To Rule Them All? *Acc. Chem. Res.* **2018**, *51* (8), 1880–1889. https://doi.org/10.1021/acs.accounts.8b00270.

(10) Gaita-Ariño, A.; Luis, F.; Hill, S.; Coronado, E. Molecular Spins for Quantum Computation. *Nat. Chem.* **2019**, *11* (4), 301–309. https://doi.org/10.1038/s41557-019-0232-y.

(11) Cornia, A.; Seneor, P. Spintronics: The Molecular Way. *Nat. Mater.* **2017**, *16* (5), 505–506. https://doi.org/10.1038/nmat4900.

(12) Chen, Y.-C.; Liu, J.-L.; Ungur, L.; Liu, J.; Li, Q.-W.; Wang, L.-F.; Ni, Z.-P.; Chibotaru, L. F.; Chen, X.-M.; Tong, M.-L. Symmetry-Supported Magnetic Blocking at 20 K in Pentagonal Bipyramidal Dy(III) Single-Ion Magnets. *J. Am. Chem. Soc.* **2016**, *138* (8),

2829–2837. https://doi.org/10.1021/jacs.5b13584.

(13) Ungur, L.; Chibotaru, L. F. Strategies toward High-Temperature Lanthanide-Based Single-Molecule Magnets. *Inorg. Chem.* **2016**, *55* (20), 10043–10056. https://doi.org/10.1021/acs.inorgchem.6b01353.

(14) Canaj, A. B.; Dey, S.; Martí, E. R.; Wilson, C.; Rajaraman, G.; Murrie, M. Insight into D6h Symmetry: Targeting Strong Axiality in Stable Dysprosium(III) Hexagonal Bipyramidal Single-Ion Magnets. *Angew. Chemie Int. Ed.* **2019**, *58* (40), 14146–14151. https://doi.org/10.1002/anie.201907686.

(15) Demir, S.; Gonzalez, M. I.; Darago, L. E.; Evans, W. J.; Long, J. R. Giant Coercivity and High Magnetic Blocking Temperatures for N23− Radical-Bridged Dilanthanide Complexes upon Ligand Dissociation. *Nat. Commun.* **2017**, *8* (1), 2144. https://doi.org/10.1038/s41467-017-01553-w.

(16) Velkos, G.; Krylov, D. S.; Kirkpatrick, K.; Spree, L.; Dubrovin, V.; Büchner, B.; Avdoshenko, S. M.; Bezmelnitsyn, V.; Davis, S.; Faust, P.; et al. High Blocking Temperature of Magnetization and Giant Coercivity in the Azafullerene Tb2@C79N with a Single-Electron Terbium–Terbium Bond. *Angew. Chemie Int. Ed.* **2019**, *58* (18), 5891–5896. https://doi.org/10.1002/anie.201900943.

(17) Gould, C. A.; McClain, K. R.; Yu, J. M.; Groshens, T. J.; Furche, F.; Harvey, B. G.; Long, J. R. Synthesis and Magnetism of Neutral, Linear Metallocene Complexes of Terbium(II) and Dysprosium(II). *J. Am. Chem. Soc.* **2019**, *141* (33), 12967–12973. https://doi.org/10.1021/jacs.9b05816.

(18) Randall McClain, K.; Gould, C. A.; Chakarawet, K.; Teat, S. J.; Groshens, T. J.; Long, J. R.; Harvey, B. G. High-Temperature Magnetic Blocking and Magneto-Structural Correlations in a Series of Dysprosium(Iii) Metallocenium Single-Molecule Magnets. *Chem. Sci.* **2018**, *9* (45), 8492–8503. https://doi.org/10.1039/C8SC03907K.

(19) Goodwin, C. A. P.; Ortu, F.; Reta, D.; Chilton, N. F.; Mills, D. P. Molecular Magnetic Hysteresis at 60 Kelvin in Dysprosocenium. *Nature* **2017**, *548*, 439.

(20) Guo, F.-S.; Day, B. M.; Chen, Y.-C.; Tong, M.-L.; Mansikkamäki, A.; Layfield, R. A. A Dysprosium Metallocene Single-Molecule Magnet Functioning at the Axial Limit. *Angew. Chemie - Int. Ed.* **2017**, *56* (38). https://doi.org/10.1002/anie.201705426.

(21) Guo, F.-S.; Day, B. M.; Chen, Y.-C.; Tong, M.-L.; Mansikkamäki, A.; Layfield, R. A. Magnetic Hysteresis up to 80 Kelvin in a Dysprosium Metallocene Single-Molecule Magnet. *Science* **2018**, *362* (6421), 1400–1403. https://doi.org/10.1126/science.aav0652.

(22) Habib, F.; Brunet, G.; Vieru, V.; Korobkov, I.; Chibotaru, L. F.; Murugesu, M. Significant Enhancement of Energy Barriers in Dinuclear Dysprosium Single-Molecule Magnets Through Electron-Withdrawing Effects. *J. Am. Chem. Soc.* **2013**, *135* (36), 13242–13245. https://doi.org/10.1021/ja404846s.

(23) Sorace, L.; Benelli, C.; Gatteschi, D. Lanthanides in Molecular Magnetism: Old Tools in a New Field. *Chem. Soc. Rev.* **2011**, *40* (6), 3092–3104. https://doi.org/10.1039/c0cs00185f.

(24) Chilton, N. F.; Anderson, R. P.; Turner, L. D.; Soncini, A.; Murray, K. S. PHI: A Powerful New Program for the Analysis of Anisotropic Monomeric and Exchange-Coupled Polynuclear d- and f-Block Complexes. *J. Comput. Chem.* **2013**, *34* (13), 1164–1175.

https://doi.org/10.1002/jcc.23234.

(25) Benelli, C.; Gatteschi, D. Magic Dysprosium. In *Introduction to Molecular Magnetism*; John Wiley & Sons, Ltd, 2015; pp 277–294. https://doi.org/10.1002/9783527690541.ch16.

(26) Dickie, C. M.; Nippe, M. Magnetization Dynamics of a Heterometallic Dy-Isocarbonyl Complex. *Inorg. Chem. Front.* **2016**, *3* (1), 97–103. https://doi.org/10.1039/c5qi00224a.

(27) Pugh, T.; Chilton, N. F.; Layfield, R. A. A Low-Symmetry Dysprosium Metallocene Single-Molecule Magnet with a High Anisotropy Barrier. *Angew. Chemie - Int. Ed.* **2016**, *55* (37). https://doi.org/10.1002/anie.201604346.

(28) Liu, S.-S.; Wang, Z.-M.; Jiang, S.-D.; Gao, S.; Wang, B.-W.; Zhou, L.-N. Series of Lanthanide Organometallic Single-Ion Magnets. *Inorg. Chem.* **2012**, *51* (5), 3079–3087. https://doi.org/10.1021/ic202511n.

(29) Roos, B. O. The Complete Active Space Self-Consistent Field Method and Its Applications in Electronic Structure Calculations. In *Advances in Chemical Physics: Ab Initio Methods in Quantum Chemistry II, Vol. 69*; Lawley, K. P., Ed.; Wiley: New York, NY, USA, 1987; pp 399–455.

(30) Siegbahn, P.; Heiberg, A.; Roos, B.; Levy, B. A Comparison of the Super-CI and the Newton-Raphson Scheme in the Complete Active Space SCF Method. *Phys. Scr.* **1980**, *21* (3--4), 323–327.

(31) Roos, B. O.; Taylor, P. R.; Siegbahn, P. E. M. A Complete Active Space SCF Method (CASSCF) Using a Density Matrix Formulated Super-CI Approach. *Chem. Phys.* **1980**, *48*

(2), 157–173. https://doi.org/10.1016/0301-0104(80)80045-0.

(32) Siegbahn, P. E. M.; Almlöf, J.; Heiberg, A.; Roos, B. O. The Complete Active Space SCF (CASSCF) Method in a Newton--Raphson Formulation with Application to the HNO Molecule. *J. Chem. Phys.* **1981**, *74* (4), 2384–2396. https://doi.org/10.1063/1.441359.

(33) Roos, B. O.; Lindh, R.; Malmqvist, P. Å.; Veryazov, V.; Widmark, P.-O. *Multiconfigurational Quantum Chemistry*; Wiley: Hoboken, NJ, USA, 2016.

(34) Malmqvist, P. Å.; Roos, B. O.; Schimmelpfennig, B. The Restricted Active Space (RAS) State Interaction Approach with Spin--Orbit Coupling. *Chem. Phys. Lett.* **2002**, *357* (3--4), 230–240. https://doi.org/http://dx.doi.org/10.1016/S0009-2614(02)00498-0.

(35) Ungur, L.; Chibotaru, L. F. Ab Initio Crystal Field for Lanthanides. *Chem. Eur. J.* **2017**, *23* (15), 3708–3718. https://doi.org/10.1002/chem.201605102.

(36) Gagliardi, L.; Lindh, R.; Karlström, G. Local Properties of Quantum Chemical Systems: The LoProp Approach. *J. Chem. Phys.* **2004**, *121* (10), 4494–4500. https://doi.org/10.1063/1.1778131.

(37) Iwahara, N.; Ungur, L.; Chibotaru, L. F. *J*-Pseudospin States and the Crystal Field of Cubic Systems. *Phys. Rev. B* **2018**, *98* (5), 54436. https://doi.org/10.1103/PhysRevB.98.054436.